Applied Catalysis B: Environmental 224 (2018) 10–16

Contents lists available at ScienceDirect

Applied Catalysis B: Environmental

journal homepage: www.elsevier.com/locate/apcatb

Research paper

Effective separation and transfer of carriers into the redox sites on Ta_3N_5/Bi photocatalyst for promoting conversion of CO_2 into CH_4

Shaomang Wang[a,b], Yuan Guan[b], Lei Lu[a], Zhan Shi[a], Shicheng Yan[a,*], Zhigang Zou[a]

[a] Eco-Materials and Renewable Energy Research Center (ERERC), College of Engineering and Applied Sciences, Nanjing University, No. 22 Hankou Road, Nanjing, Jiangsu 210093, PR China
[b] School of Environment and Safety Engineering, School of Petrochemical Engineering, School of Huai De, Changzhou University, Changzhou 213164, PR China

ARTICLE INFO

Keywords:
Artificial photosynthesis
CH_4
CO_2 reduction
Ta_3N_5/Bi

ABSTRACT

Improving separation efficiency of carriers and inhibiting the inverse reaction are key challenges for achieving efficient sunlight driven conversion of CO_2 by H_2O as reducing agent into CH_4. Here, we proposed using metal Bi with low work function to modify *n*-type Ta_3N_5, thus building an ohmic junction photocatalyst of Ta_3N_5/Bi. It achieved an about 5 times increase in CH_4 yield compared with Ta_3N_5. The enhanced photocatalytic activity was ascribed to the following two effects: (1) The junction electric field drove the injection of conduction-band electrons of Ta_3N_5 to Bi, greatly improving separation efficiency of carriers; (2) The oxidation and reduction reaction sites were respectively constructed over Ta_3N_5 and Bi, effectively separating the oxidation reaction of H_2O and the reduction reaction of CO_2, which distinctly suppressed the reverse reaction during CH_4 generation.

1. Introduction

Photocatalytic reduction of CO_2 by H_2O into CH_4 is a promising solar conversion and storage technique [1–10]. This energy conversion route is achieved by two half-reactions [11–16]. Firstly, H_2O is oxidized by photo-induced holes in the valence band (VB) of semiconductor photocatalyst to generate hydrogen ions via the reaction of $4H_2O + 8h^+ \rightarrow 2O_2 + 8H^+$ ($E^o_{ox} = 0.82$ V vs. normal hydrogen electrode, NHE). Secondly, CO_2 is reduced by photo-generated electrons in the conduction band (CB) of semiconductor photocatalyst into CH_4 via the reaction of $CO_2 + 8e + 8H^+ \rightarrow CH_4 + 2H_2O$ ($E^o_{red} = -0.24$ V vs NHE). Therefore, the photocatalyst with excellent ability in separating carriers and suppressing the inverse reaction is needed for efficient solar energy conversion.

Tantalum nitride (Ta_3N_5) has received increasing attention because it exhibited good photocatalytic activity in water splitting and degradation of organic pollutants [17–28]. The CB and VB energy level for Ta_3N_5 are about −0.29 and 1.81 V vs. reversible hydrogen electrode (RHE), which meets the thermodynamic requirements for photocatalytic reduction of CO_2 by H_2O into CH_4. Modifying Ta_3N_5 by metal particles is a facile route to improve the separation efficiency of carriers [29–32]. For example, after the modification of Pt particles, a surface band bending upward at junction region between *n*-type Ta_3N_5 and metal particles is formed for reaching the thermodynamic equilibrium, owing to that work function of Pt (5.7 eV) is higher than that of Ta_3N_5 (4.5 eV) [33]. The band bending upward will obstruct the injection of conduction-band electrons of Ta_3N_5 into Pt particles, where usually are the catalytic reduction sites with low over-potential. This means that, when the work function of semiconductor is lower than that of metal, transferring the electrons in the CB of semiconductor into metal particles is highly depending on the height of Schottky barrier. Although high height of Schottky barrier means large band bending which greatly enhances the charge separation, the higher electron energy was required to cross the barrier for transferring electrons into metal particles. Thus, a surface band bending downward is expected for facilitating electron injection into metal particles.

Here, metal Bi was selected to modify the Ta_3N_5 due to its low work function. It can be predicted that the surface band bending downward will be formed at the interface junction region between Bi and Ta_3N_5, resulting from that the work function of Bi (4.2 eV) is lower than that of Ta_3N_5 (4.5 eV). The surface band bending downward facilitates transferring the conduction-band electrons of Ta_3N_5 into Bi particles. To verify this hypothesis, we have synthesized the Ta_3N_5/Bi composite photocatalyst by directly nitriding $BiTaO_4$, achieving an about 5 times increase in CH_4 yield. The enhanced photocatalytic activity can be attributed to the enhanced electron transfer from Ta_3N_5 to Bi and the effective separation of the redox sites. Theoretical calculations indicate that the H_2O and CO_2 tend to activate on surface of Ta_3N_5 and Bi, respectively, inducing the separation of the redox sites. For the CO_2 reduction into CH_4, 8-electron transfer is needed. This means that CH_4

* Corresponding author.
E-mail address: yscfei@nju.edu.cn (S. Yan).

http://dx.doi.org/10.1016/j.apcatb.2017.10.043
Received 24 June 2017; Received in revised form 29 September 2017; Accepted 15 October 2017
Available online 16 October 2017

generation is slow kinetically. A possible reverse reaction is the degradation of reduced carbon-containing intermediate species by photogenerated holes. Therefore, spatially separated reaction sites were beneficial to suppress the possible reverse reaction during the CH_4 generation. The proposed strategy may offer a new route to design the efficient photocatalysts for solar energy conversion.

2. Experimental section

2.1. Photocatalyst preparation

To synthesize the Ta_3N_5/Bi composite photocatalyst, the $BiTaO_4$ was first fabricated by molten-salt method [34]. Typically, 0.51 g of Bi_2O_3 and 0.48 g of Ta_2O_5 with the eutectic molten salt (0.32 g of NaCl and 0.41 g of KCl) were fully ground for 30 min after adding 5 mL of ethanol. The mixture was dried at 80 °C for 2 h and then calcined at 850 °C for 5 h with a heating rate of 5 °C min^{-1} in a muffle furnace. After the furnace was naturally cooled to room temperature, the product was washed with deionized water, filtrated and dried at 80 °C for 4 h. Ta_3N_5/Bi was synthesized by heating $BiTaO_4$ under ammonia atmosphere. In a typical experiment, 1 g of $BiTaO_4$ powders were uniformly dispersed on the bottom of an alumina crucible, and then calcined in a tube furnace (inner diameter 50 mm) at 750 °C for 10 h with a heating rate of 10 °C min^{-1} under 500 mL min^{-1} flowing NH_3. The sample was naturally cooled to room temperature. Using the similar nitriding procedure, Ta_3N_5/Bi with different molar ratio of Bi/Ta was prepared by adjusting the amount of Bi_2O_3 and Ta_2O_5. For comparison, the Ta_3N_5 was prepared by nitriding the Ta_2O_5 using the above-mentioned procedure. A mixture of Ta_3N_5 and Bi (M-Ta_3N_5/Bi) was fabricated via heating the mixture of Bi_2O_3 (0.51 g) and Ta_2O_5 (0.48 g) with the similar nitridation procedure for preparing Ta_3N_5/Bi.

2.2. Characterization

The crystal structures of the samples were identified by powder X-ray diffraction (XRD) (Rigaku Ultima III, Japan) with Cu Kα radiation (λ = 1.5418 Å). The scanning electron microscope (SEM) images were collected on FEI NOVA Nano SEM 230. The elemental compositions of the samples were analyzed by X-ray energy dispersive spectroscopy (EDS). Transmission electron microscope (TEM) characterizations were performed on JEM-200CX. X-ray photoelectron spectroscopy (XPS) studies were conducted on a PHI5000 Versa Probe (ULVAC-PHI, Japan) with monochromatized Al Kα X-ray radiation (1486.6 eV). The optical absorption spectra were recorded on a UV–vis diffuse reflection spectrophotometer (UV–vis DRS 2550, Shimadzu). The photoluminescence spectra (PL) were obtained via Fluoromax-4 (HORIBA, USA) with an excitation wavelength at 450 nm. Photoelectrochemical measurements were performed on an electrochemical analyzer (CHI-660D, Shanghai Chenhua, China) in a standard three-electrode system with a bias potential of 0.23 V vs. saturated calomel electrode. A platinum wire and a saturated calomel electrode were used as counter electrode and reference electrode, respectively. Working electrode was prepared as follows: 30 mg of the sample and 10 mg of iodine were added to 25 mL of acetone with ultrasonic shock for half an hour. Then, the sample was deposited on a fluorine-doped tin oxide conducting substrate with a fixed area of 1 cm^2 by a voltage of 15 V for 5 min. NaOH (1 mol L^{-1}) aqueous solution was utilized as the electrolyte. A 500 W Xe lamp was used as the light source for photocurrent measurement.

2.3. Evaluation of photocatalytic activity

The photocatalytic reactions were performed in a gas sealed container with a volume of 230 mL (Fig. S1). The as-prepared photocatalyst (0.1 g) was uniformly dispersed on a quartz disk with an area of 4.20 cm^2. After the reaction container was evacuated, CO_2 was purged with initial pressure of about 705 bar and then 0.4 mL of deionized water was injected into the reaction container. The system was kept in the dark for 2 h to ensure that the adsorption-desorption equilibrium was established between gaseous molecules and the photocatalyst. A 300 W Xenon arc lamp was used as light source. During the irradiation, 1 mL of gas withdrawn from the above system was analyzed by a GC-2014 (Shimadzu, Japan) gas chromatograph every hour.

2.4. Computational methods

The Cambridge Sequential Total Energy Package (CASTEP) code was used to perform the density functional theory (DFT) computations. The general gradient approximation (GGA) with PBE was used to describe the exchange-correlation eff ; ;ects for the calculations of work function and adsorption energy. The attractive energy between nuclear and electrons was calculated by ultrasoft pseudo-potential. The convergence threshold of geometric optimization was set at 2.0×10^{-5} eV $atom^{-1}$ for total energy, 0.05 eV $Å^{-1}$ for maximum force, 0.1 GPa for stress and 0.002 Å for maximum displacement. For the calculations of work function, the structure of Bi (024) was built including 5 atoms of Bi, and lattice parameter was a = 6.0 Å, b = 12.7 Å, c = 23.1 Å and α = β = γ = 90°. The structure of Ta_3N_5 (023) contained 18 atoms of Ta and 30 atoms of N, and lattice parameter was a = 18.5 Å, b = 3.9 Å, c = 28.2 Å, α = β = 90° and γ = 84°. For the calculations of adsorption energy, the interface structure of Ta_3N_5 (023)/Bi (024) was constructed including 12 atoms of Ta, 20 atoms of N and 4 atoms of Bi, and lattice parameter was a = 18.8 Å, b = 8.7 Å, c = 15.9 Å, α = β = 90° and γ = 87° (Fig. S2).

3. Results and discussion

The XRD patterns of Ta_3N_5, Ta_3N_5/Bi and M-Ta_3N_5/Bi are presented in Fig. 1a. The XRD peaks of sample prepared by nitriding Ta_2O_5 can be assigned to the single-phase Ta_3N_5 with orthorhombic structure (JCPDS card No.79-1533). Ta_3N_5/Bi and M-Ta_3N_5/Bi clearly exhibited the XRD patterns of Ta_3N_5 and hexagonal Bi (JCPDS card No.85-1329), demonstrating that $BiTaO_4$ or a mixture of Ta_2O_5 and Bi_2O_3 can be converted to Ta_3N_5 and metal Bi after being calcined at 750 °C for 10 h under a NH_3 flow of 500 mL min^{-1}. This means that the phase separation, formation of Ta_3N_5 and Bi metal particles, occurs during the nitridation of $BiTaO_4$ due to the strong reducibility of NH_3 at high temperature. Indeed, under the same conditions, the Bi_2O_3 powders can be completely reduced into Bi metal particles (Fig. S3).

Fig. 1b–d present the chemical states of Bi, Ta and N. The binding energies of Bi $4f_{7/2}$ and Bi $4f_{5/2}$ in the Ta_3N_5/Bi were 158.1 and 163.4 eV, which were about 1 eV higher than those in the metal Bi (Bi $4f_{7/2}$ = 157.1 and Bi $4f_{5/2}$ = 162.4 eV), and were about 2.4 eV lower than those in the Bi_2O_3 (Bi $4f_{7/2}$ = 159.5 and Bi $4f_{5/2}$ = 164.9 eV) [35]. In addition, the binding energies of Ta $4f_{7/2}$, Ta $4f_{5/2}$ and N 1 s were 24.0, 25.7 and 395.4 eV in the Ta_3N_5/Bi, respectively, which were slightly lower than those of Ta $4f_{7/2}$ (24.2 eV), Ta $4f_{5/2}$ (25.9 eV) and N 1 s (395.6 eV) in the Ta_3N_5. For Ta_3N_5/Bi, the binding energy increment for Bi and decrease for Ta and N would reflect that the surface band bending downward formed, resulting from the electron transfer from Bi to Ta_3N_5 for building up thermodynamic equilibrium. However, no obvious changes in binding energies for Bi, Ta and N in the M-Ta_3N_5/Bi were observed if compared to Ta_3N_5 and Bi metal (Fig. S4), confirming that the Ta_3N_5/Bi composite photocatalyst prepared by nitriding $BiTaO_4$ is beneficial to form a high-quality Ta_3N_5-Bi junction interface with strong interaction.

Scanning electron microscopy (SEM) and transmission electron microscopy (TEM) observations were performed to visualize the morphology and interface structure between Ta_3N_5 and Bi. As shown in Fig. 2a, the Ta_3N_5 obtained by nitriding Ta_2O_5 exhibited the porous particles with apparent size of 500–800 nm, well consistent with the previous reports [25]. After nitriding, the $BiTaO_4$ plate (Fig. 2b) was converted to a porous plate composed of Ta_3N_5 nanoparticles with

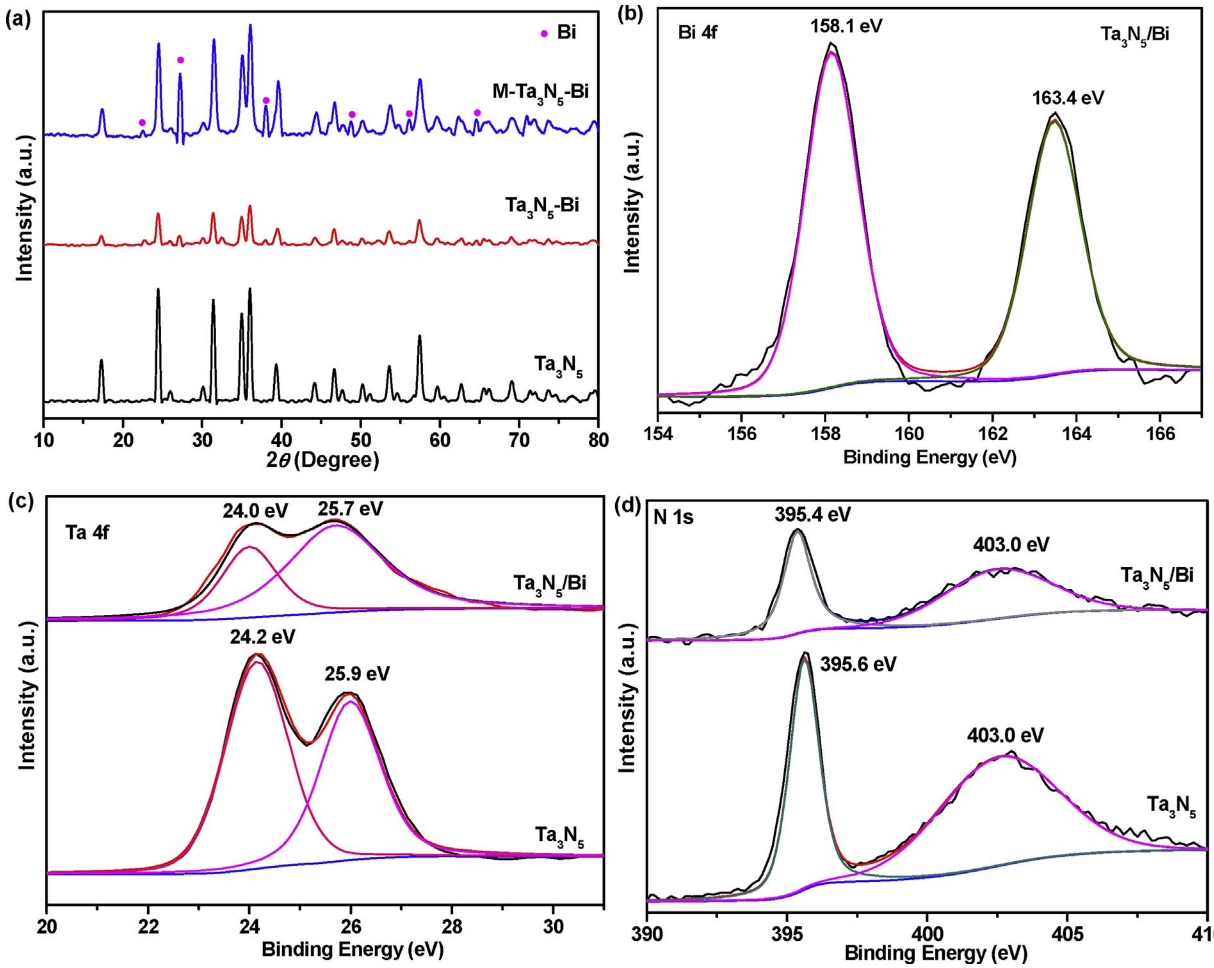

Fig. 1. (a) XRD patterns of Ta_3N_5, Ta_3N_5/Bi and M-Ta_3N_5/Bi. XPS core-level spectra of (b) Bi 4f, (c) Ta 4f and (d) N 1s.

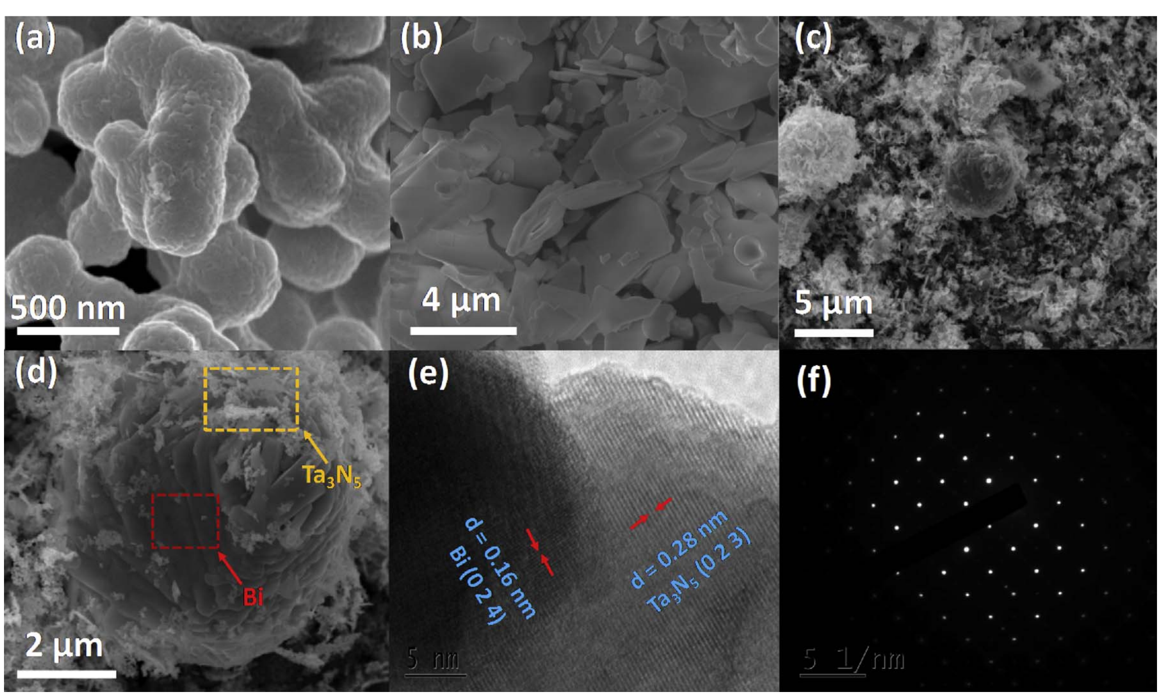

Fig. 2. SEM images of (a) Ta_3N_5, (b) $BiTaO_4$ and (c and d) Ta_3N_5/Bi. (e) TEM image of Ta_3N_5/Bi. (f) SAED pattern of Ta_3N_5/Bi.

particle size of 50–100 nm (Fig. 2c and d, and Fig. S5a). In addition, the large agglomerate microspheres of about 5–6 μm were observed in the products (Fig. 2c and d), which can be assigned to the Bi metal by energy dispersive spectrometry (EDS) analysis (Fig. S5b). A lot of porous Ta_3N_5 plate tightly anchored on Bi microspheres. These evidences imply that the Ta_3N_5 plate inherits the apparent profile of $BiTaO_4$ precursor and porous structure originates from the phase separation of Bi metal. At the high temperature, the Bi metal tends to agglomerate into larger particles due to its low melting point (271.3 °C). However, the high-resolution TEM lattice image clearly revealed the smooth particle interface between (024) facet of Bi and (023) facet of Ta_3N_5 (Fig. 2e). This fact means that the Bi metal nanoparticles except the large agglomerate particles exist in the porous framework of Ta_3N_5 with high-quality interface with Ta_3N_5. Indeed, selected area electron diffraction on the particle interface confirms that both Ta_3N_5 and Bi nanoparticles are single crystal (Fig. 2f). SEM analysis indicates that larger Bi microspheres (about 7–8 μm) and Ta_3N_5 nanoparticles (about 200–300 nm) formed in the M-Ta_3N_5/Bi (Fig. S6a).

As confirmed by XPS, the weak interaction between Ta_3N_5 and Bi particles in the M-Ta_3N_5/Bi may be attributed to that the larger particle size of Ta_3N_5 and Bi and the particle contact achieved by sintering effect, not similar to the simultaneous phase separation of Bi and Ta_3N_5 from $BiTaO_4$ inducing the high-quality interface. Obviously, for the M-Ta_3N_5/Bi, the particle size of Ta_3N_5 is significantly smaller than that of Ta_2O_5 precursor (about 500–800 nm) (Fig. S6b). This is due to that the Bi flux formed during the nitridation, which plays the flux role in the nucleation and growth of Ta_3N_5 crystal.

UV–vis absorption spectra display that Ta_3N_5, Ta_3N_5/Bi and M-Ta_3N_5/Bi exhibited the slight difference in optical absorption edge to be around 603–605 nm (Fig. 3a), resulting from the band gap excitation from N 2p orbitals to Ta 5d orbitals. For Ta_3N_5/Bi and M-Ta_3N_5/Bi, an enhanced background absorption was observed in the wavelength longer than 600 nm, which can be ascribed to the light absorption of Bi metal (Fig. S7). The CO_2 reduction was carried out in CO_2 and H_2O vapor system under 300 W Xe lamp light irradiation. As shown in Fig. S8, the photocatalytic activity of Ta_3N_5/Bi gradually enhanced with increasing molar ratio of Bi/Ta. The optimal molar ratio of Bi/Ta was 1. After 8 h light irradiation, metal Bi powders obtained by nitriding Bi_2O_3 exhibited almost no photocatalytic activity for CO_2 reduction into CH_4 (Fig. 3b and c). And the total CH_4 generation is about 0.89 for Ta_3N_5, 1.14 for M-Ta_3N_5/Bi and 4.52 μmol $g_{catalyst}{}^{-1}$ for Ta_3N_5/Bi, respectively. Obviously, the CH_4 generation rate over Ta_3N_5/Bi (0.57 μmol $g_{catalyst}{}^{-1}$ h^{-1}) is about 5.2 and 4.1 times higher than those over Ta_3N_5 (0.11 μmol g^{-1} h^{-1}) and M-Ta_3N_5/Bi (0.14 μmol g^{-1} h^{-1}), respectively. The same experiments of CO_2 reduction performed in the dark or in the absence of the photocatalysts showed no appearance of CH_4, indicating that the reaction of CO_2 reduction is driven by light with the photocatalysts. Isotope labeling experiment was conducted by using $^{13}CO_2$. $^{13}CH_4$ signal was detected by gas chromatography-mass spectrometry in the gas products (Fig. S9). This confirms that CH_4 formation originates from photocatalytic reduction of CO_2.

The specific surface area and average pore diameter analyzed by N_2 adsorption-desorption were 9.1 cm^2 g^{-1} and 11.1 nm for Ta_3N_5, 6.0 cm^2 g^{-1} and 7.7 nm for M-Ta_3N_5/Bi, and 11.8 cm^2 g^{-1} and 15.2 nm for Ta_3N_5/Bi (Fig. S10). The Ta_3N_5/Bi exhibited a similar specific surface area to the Ta_3N_5. Therefore, the difference in CH_4 generation rate does not result from the difference in specific surface area. A 615 nm emission peak, near to the absorption edge at about 603–605 nm, was observed in photoluminescence (PL) spectra of these as-prepared Ta_3N_5 samples, which would originate from the band edge recombination. The PL peak intensity is in the order of Ta_3N_5 > M-Ta_3N_5/Bi > Ta_3N_5/Bi (Fig. 4a), indicating that the modifying Ta_3N_5 by metal Bi can effectively decrease the carrier recombination. In particular, the low PL peak intensity for Ta_3N_5/Bi would mean that the high-quality interface between Bi and Ta_3N_5 with the band bending downward is greatly contributable to the charge separation, thus decreasing their recombination. As displayed in Fig. 4b, the steady-state photocurrent exhibited the order of Ta_3N_5/Bi > M-Ta_3N_5/Bi > Ta_3N_5, confirming the highest separation efficiency of Ta_3N_5/Bi, in good agreement with PL results.

To obtain the nature of charge separation at the interface between Bi and Ta_3N_5, surface slab model for (024) facet of Bi (Fig. 5a) and (023) facet of Ta_3N_5 (Fig. 5c), well consistent with the TEM observations, was built to calculate their surface work functions. Surface potential analysis (Fig. 5b and d) demonstrated that the work function of Bi (024) was approximately 4.02 eV, which was evidently lower than 4.95 eV for Ta_3N_5 (023). When the Bi (024) contacted with Ta_3N_5 (023), the electrons of Bi (024) will diffuse to Ta_3N_5 (023) until they share the same Fermi level. A built-in electric field with the direction from the surface to bulk is constructed on the side of Ta_3N_5. This makes the surface energy band of Ta_3N_5 bend downward [33]. Under irradiation, electrons from space charge layer of Ta_3N_5 are driven by built-in electric field to Bi and then react with CO_2, which process greatly inhibits the carrier recombination of Ta_3N_5/Bi (Fig. 6). Compared to M-Ta_3N_5/Bi, the electron migration-efficiency of Ta_3N_5/Bi from Ta_3N_5 to Bi is higher due to the smooth interface between Ta_3N_5 and Bi formed during in situ crystal growth. Thence, carrier-separation efficiency of Ta_3N_5/Bi is significantly higher than those of M-Ta_3N_5/Bi and Ta_3N_5.

To further verify that the electrons of Bi will move toward Ta_3N_5 when they were in contact under dark. An interface model of Ta_3N_5 (023)/Bi (024) was built (Fig. S2). Electron density difference clearly showed that the Bi atoms lost electrons and Ta_3N_5 gained electrons (Fig. 7), well consistent with the XPS analysis. At Ta_3N_5 (023)/Bi (024) interface, a Bi atom averagely offers 0.67 electrons for Ta_3N_5. It confirms that the electrons of Bi will migrate to Ta_3N_5 under dark until they share the same Fermi level.

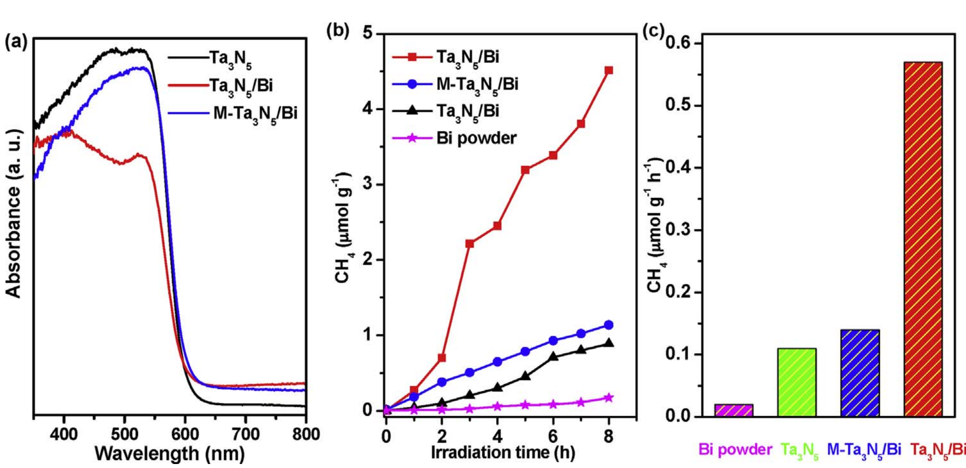

Fig. 3. (a) UV–vis diffuse reflectance spectra of Ta_3N_5, Ta_3N_5/Bi and M-Ta_3N_5/Bi. (b) Photocatalytic CH_4 evolution amount over Ta_3N_5, Ta_3N_5/Bi, M-Ta_3N_5/Bi and Bi powers as a function of irradiation time. (c) Average yield of CH_4 over Ta_3N_5, Ta_3N_5/Bi, M-Ta_3N_5/Bi and Bi powers.

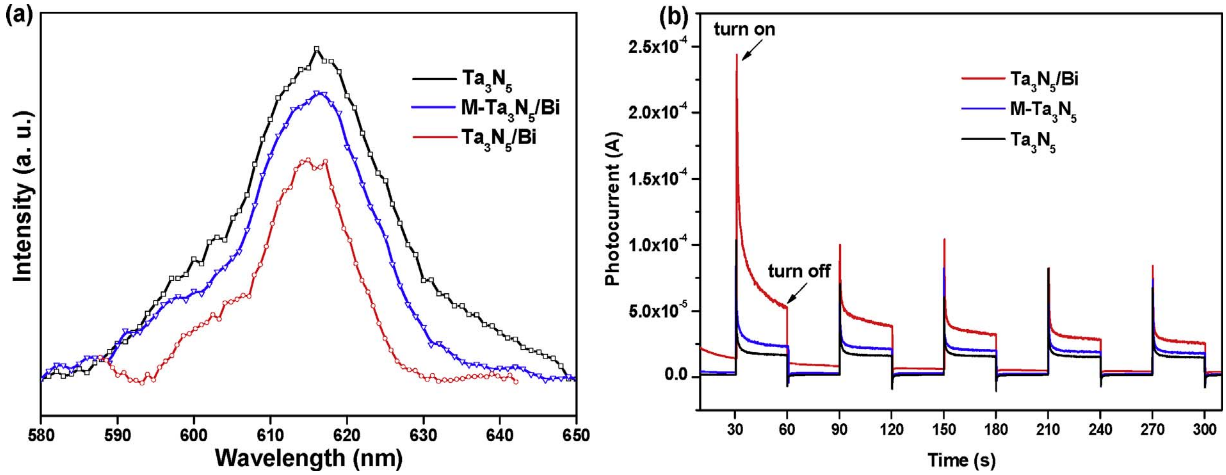

Fig. 4. (a) Photoluminescence spectra of Ta_3N_5, Ta_3N_5/Bi and M-Ta_3N_5/Bi. (b) Photocurrents of Ta_3N_5, Ta_3N_5/Bi and M-Ta_3N_5/Bi.

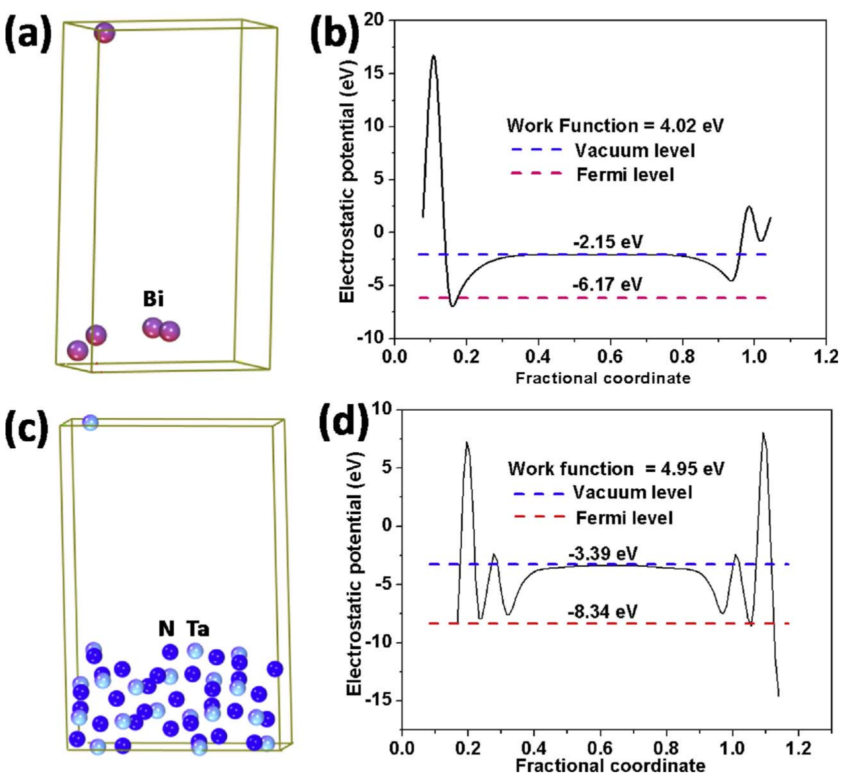

Fig. 5. The surface slab models and work functions of (a and b) Bi (024) and (c and d) Ta_3N_5 (023).

To verify above proposed redox sites, adsorption energy and geometric parameter change before and after adsorption of CO_2 and H_2O over different surface of Ta_3N_5 (023)/Bi (024) were calculated. Adsorption energy of an adsorbate over a photocatalyst can be calculated by the following Eq. (1).

$$E_{ads} = E_{ads/pho} - (E_{pho} + E_{adsorbate}) \quad (1)$$

E_{ads} is adsorption energy. $E_{ads/pho}$, E_{pho} and $E_{adsorbate}$ are energy of adsorption system, energy of a photocatalyst and energy of an adsorbate, respectively. The calculated results are illustrated in Fig. 8 and Table 1.

For H_2O adsorption over Ta_3N_5 (023)/Bi (024), E_{ads} of H_2O over Ta_3N_5 (023) and Bi (024) were −2 eV and −1.7 eV, respectively. The bond length of H_2O and the H—O—H bond angle were 0.975 Å and 105.2° over Ta_3N_5 (023) and Bi (024) before adsorption. After the adsorption reached a steady state, the bond length of H_2O over Ta_3N_5 (023) and Bi (024) was 0.983 Å and 0.978 Å, respectively. The H—O—H bond angle over Ta_3N_5 (023) and Bi (024) was 107.4° and 104.1°, respectively. The E_{ads}, bond length of H_2O and the H—O—H bond angle over Ta_3N_5 (023) were greater than those over Bi (024) after the adsorption reached a steady state.

For CO_2 adsorption over Ta_3N_5 (023)/Bi (024), E_{ads} of CO_2 over Ta_3N_5 (023) and Bi (024) were −1.8 eV and −2.2 eV, respectively. The bond length of CO_2 and the O═C═O bond angle were 1.182 Å and 178.3° over Ta_3N_5 (023) and Bi (024) before adsorption. After the adsorption reached a steady state, the bond length of CO_2 over Ta_3N_5 (023) and Bi (024) was 1.181 Å and 1.186 Å, respectively. The O═C═O bond angle over Ta_3N_5 (023) and Bi (024) was 178.5° and 178.6°, respectively. The E_{ads}, bond length of CO_2 and the O═C═O bond angle over Ta_3N_5 (023) were smaller than those over Bi (024) after the adsorption reached a steady state. The results clearly suggest that H_2O is oxidized over Ta_3N_5 and CO_2 is reduced over Bi. The stability test of the photocatalyst has been carried out (Fig. S11). After cycling reaction three times, the CH_4 yield over the reused photocatalyst remained

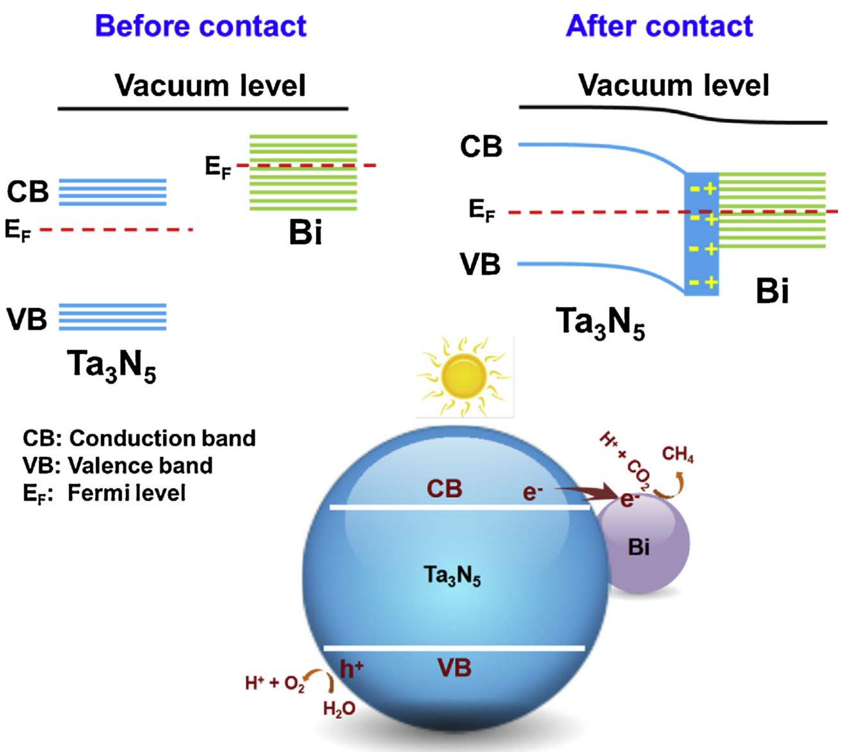

Fig. 6. Schematic illustration of the ohmic-junction formation between Ta_3N_5 and Bi, and CH_4 evolution over Ta_3N_5/Bi.

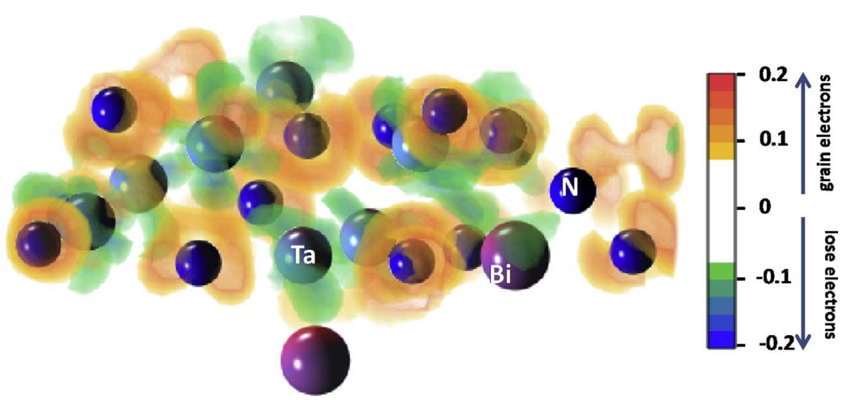

Fig. 7. Electron density difference of Ta_3N_5 (023)/Bi (024).

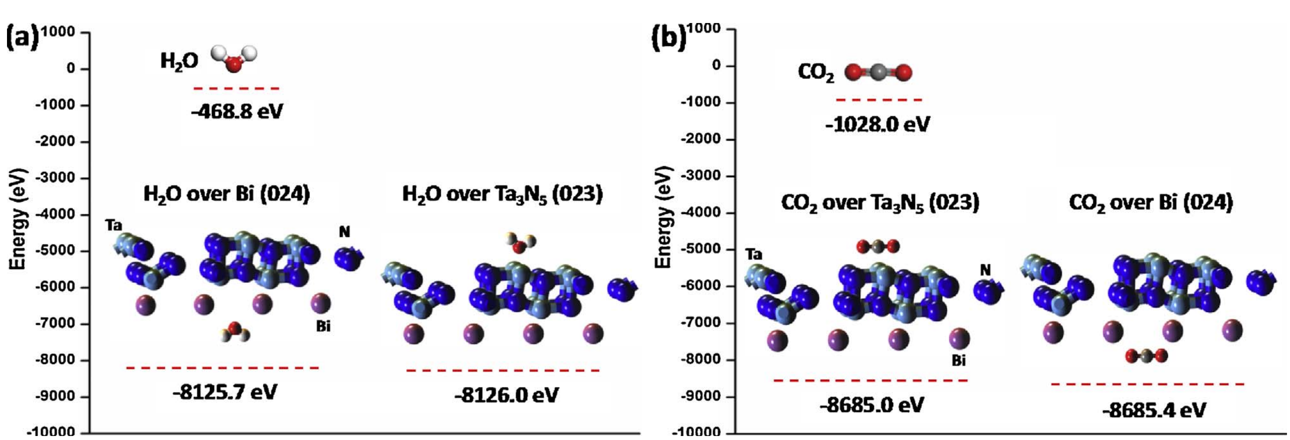

Fig. 8. (a) The energies of H_2O, H_2O over Ta_3N_5 (023) and H_2O over Bi (024). (b) The energies of CO_2, CO_2 over Ta_3N_5 (023) and CO_2 over Bi (024). The energy of Ta_3N_5 (023)/Bi (024) calculated was −7655.2 eV.

Table 1
Adsorption energy and geometric parameter change before and after adsorption of H_2O and CO_2 over different surface of Ta_3N_5 (023)/Bi (024).

	H_2O over Ta_3N_5 (023)		H_2O over Bi (024)	
	Before adsorption	After adsorption	Before adsorption	After adsorption
E_{ads}/eV	–	−2.0	–	−1.7
d_{O-H}/Å	0.975	0.983	0.975	0.978
∠(HOH)/°	105.2	107.4	105.2	104.1
	CO_2 over Ta_3N_5 (023)		CO_2 over Bi (024)	
	Before adsorption	After adsorption	Before adsorption	After adsorption
E_{ads}/eV	–	−1.8	–	−2.2
$d_{C=O}$/Å	1.182	1.181	1.182	1.186
∠(OCO)/°	178.3	178.5	178.3	178.6

above 91% of that over the fresh sample, exhibiting the excellent stability of Bi/Ta_3N_5 photocatalyst.

4. Conclusions

In summary, a composite catalyst of Ta_3N_5/Bi with excellent photocatalytic activity for CO_2 reduction into CH_4 was successfully prepared by heating $BiTaO_4$ in an ammonia atmosphere. Bi metal particles obviously improved carrier-separation efficiency of Ta_3N_5. Ta_3N_5 was the catalytic oxidation site and Bi was the catalytic reduction site, thus effectively inhibiting the inverse reaction during CH_4 generation. Our work provided a promising strategy for designing and developing highly efficient photocatalysts of CO_2 conversion.

Acknowledgments

This work was supported primarily by the National Basic Research Program of China (2013CB632404), the National Natural Science Foundation of China (51572121, 21603098, 21633004 and 11504162), the State Key Laboratory of NBC Protection for Civilian (SKLNBC2014-09), the Natural Science Foundation of Jiangsu Province (BK20151265, BK20150580 and BK20161277), the Natural Science Foundation of Jiangsu Education Department (16KJB610002), the Postdoctoral Science Foundation of China (2017M611784) and the Fundamental Research Funds for the Central Universities (021314380084). We are grateful to the High Performance Computing Center (HPCC) of Nanjing University for doing the numerical calculations in this paper on its IBM Blade cluster system.

Appendix A. Supplementary data

Supplementary data associated with this article can be found, in the online version, at http://dx.doi.org/10.1016/j.apcatb.2017.10.043.

References

[1] S.N. Habisreutinger, L. Schmidt-Mende, J.K. Stolarczyk, Angew. Chem. Int. Ed. 52 (2013) 7372–7408.
[2] Y.T. Liang, B.K. Vijayan, K.A. Gray, M.C. Hersam, Nano Lett. 11 (2011) 2865–2870.
[3] F. Sastre, A.V. Puga, L.C. Liu, A. Corma, H. Garcia, J. Am. Chem. Soc. 136 (2014) 6798–6801.
[4] I. Shown, H.C. Hsu, Y.C. Chang, C.H. Lin, P.K. Roy, A. Ganguly, C.H. Wang, J.K. Chang, C.I. Wu, L.C. Chen, K.H. Chen, Nano Lett. 14 (2014) 6097–6103.
[5] B. Mei, A. Pougin, J. Strunk, J. Catal. 306 (2013) 184–189.
[6] Y.F. Xu, M.Z. Yang, B.X. Chen, X.D. Wang, H.Y. Chen, D.B. Kuang, C.Y. Su, J. Am. Chem. Soc. (2017).
[7] R. Long, Y. Li, Y. Liu, S.M. Chen, X.S. Zheng, C. Gao, C.H. He, N.S. Chen, Z.M. Qi, L. Song, J. Jiang, J.F. Zhu, Y.J. Xiong, J. Am. Chem. Soc. 139 (2017) 4486–4492.
[8] W.K. Wang, D.F. Xu, B. Cheng, J.G. Yu, C.J. Jiang, J. Mater. Chem. A 5 (2017) 5020–5029.
[9] Y. Ji, Y. Luo, J. Am. Chem. Soc. 138 (2016) 15896–15902.
[10] C. Dong, M. Xing, J. Zhang, Mater. Horiz. 3 (2016) 608–612.
[11] S.C. Yan, S.X. Ouyang, J. Gao, M. Yang, J.Y. Feng, X.X. Fan, L.J. Wan, Z.S. Li, J.H. Ye, Y. Zhou, Z.G. Zou, Angew. Chem. Int. Ed. 49 (2010) 6400–6404.
[12] P. Li, Y. Zhou, Z.Y. Zhao, Q.F. Xu, X.Y. Wang, M. Xiao, Z.G. Zou, J. Am. Chem. Soc. 137 (2015) 9547–9550.
[13] W.G. Tu, Y. Zhou, Z.G. Zou, Adv. Mater. 26 (2014) 4607–4626.
[14] V.P. Indrakanti, J.D. Kubicki, H.H. Schobert, Energ. Environ. Sci. 2 (2009) 745–758.
[15] Y. Ma, X. Wang, Y. Jia, X. Chen, H. Han, C. Li, Chem. Rev. 114 (2014) 9987–10043.
[16] Q. Liu, Y. Zhou, J.H. Kou, X.Y. Chen, Z.P. Tian, J. Gao, S.C. Yan, Z.G. Zou, J. Am. Chem. Soc. 132 (2010) 14385–14387.
[17] Y.B. Li, T. Takata, D. Cha, K. Takanabe, T. Minegishi, J. Kubota, K. Domen, Adv. Mater. 25 (2013) 125–131.
[18] S.S.K. Ma, K. Maeda, T. Hisatomi, M. Tabata, A. Kudo, K. Domen, Chem-Eur J. 19 (2013) 7480–7486.
[19] E. Nurlaela, S. Ould-Chikh, I. Llorens, J.L. Hazemann, K. Takanabe, Chem. Mater. 27 (2015) 5685–5694.
[20] L. Wang, N.T. Nguyen, X.M. Zhou, I. Hwang, M.S. Killian, P. Schmuki, Chemsuschem 8 (2015) 2615–2620.
[21] R. Gao, S.X. Zhou, M. Chen, L.M. Wu, J. Mater. Chem. 21 (2011) 17087–17090.
[22] L. Yuliati, J.H. Yang, X.C. Wang, K. Maeda, T. Takata, M. Antonietti, K. Domen, J. Mater. Chem. 20 (2010) 4295–4298.
[23] S. Khan, M.J.M. Zapata, D.L. Baptista, R.V. Goncalves, J.A. Fernandes, J. Dupont, M.J.L. Santos, S.R. Teixeira, J. Phys. Chem. C 119 (2015) 19906–19914.
[24] X.J. Feng, T.J. LaTempa, J.I. Basham, G.K. Mor, O.K. Varghese, C.A. Grimes, Nano Lett. 10 (2010) 948–952.
[25] S.S.K. Ma, T. Hisatomi, K. Maeda, Y. Moriya, K. Domen, Am. Chem. Soc. 134 (2012) 19993–19996.
[26] T. Hisatomi, M. Otani, K. Nakajima, K. Teramura, Y. Kako, D.L. Lu, T. Takata, J.N. Kondo, K. Domen, Chem. Mater. 22 (2010) 3854–3861.
[27] J. Cao, L. Ren, N. Li, C. Hu, M. Cao, Chem-Eur J. 19 (2013) 12619–12623.
[28] R. Gao, S. Zhou, M. Chen, L. Wu, J. Mater. Chem. 21 (2011) 17087–17090.
[29] S. Chen, Y. Qi, Q. Ding, Z. Li, J. Cui, F. Zhang, C. Li, J. Catal. 339 (2016) 77–83.
[30] S. Li, L. Zhang, H. Wang, Z. Chen, J. Hu, K. Xu, J. Liu, Sci. Rep. 4 (2014) 3978.
[31] B.A. Pinaud, P.C.K. Vesborg, T.F. Jaramillo, J. Phys. Chem. C 116 (2012) 15918–15924.
[32] S.J. Li, J.L. Zhang, S.W. Hu, K.B. Xu, W. Jiang, J.S. Liu, J. Alloy Compd. 695 (2017) 1137–1144.
[33] S. Bai, J. Jiang, Q. Zhang, Y. Xiong, Chem. Soc. Rev. 44 (2015) 2893–2939.
[34] Y.D. Hu, G. Chen, C.M. Li, Y.S. Zhou, J.X. Sun, S. Hao, Z.H. Han, J. Mater. Chem. A 4 (2016) 5274–5281.
[35] W.J.S.W.E. Morgan, J.R. Vanwazer, Inorg. Chem. 12 (1973) 953–955.